Effects of Design and Hydrodynamic Parameters on Optimized Swimming for Simulated, Fish-inspired Robots

Donghao Li¹, Hankun Deng¹, Yagiz E. Bayiz¹, Bo Cheng¹, Member, IEEE

Abstract—In this work, we developed a mathematical model and a simulation platform for a fish-inspired robotic template, namely Magnetic, Modular, Undulatory Robot (µBot). Through this platform, we systematically explored the effects of robot design and fluid parameters on swimming performance via reinforcement learning. The mathematical model was composed of two interacting subsystems, the robotic dynamic model and the hydrodynamic model. The hydrodynamic model consisted of the reactive components (added-mass force and pressure forces) and the resistive components (drag and friction forces). These components were nondimensionalized for deriving key "control parameters" of the robot-fluid interaction. The µBots were actuated via magnetic actuators controlled with harmonic voltage signals, which were optimized via EM-based Policy Hyper Parameter Exploration (EPHE) to maximize forward swimming speed. By varying the control parameters, a total of 36 cases with different robot template variations (Number of Actuators (NoA) and stiffness) and hydrodynamic parameters were simulated and optimized via EPHE. Results showed that the wavelength of the optimized gaits (i.e., backward traveling wave along the body) was independent of template variations and hydrodynamic parameters. Higher NoA yielded higher speed but lower speed per body length, suggesting a diminishing gain from added actuators. Body and caudal-fin dynamics were dominated by the interaction among fluid added-mass, spring, and actuation torque, with negligible contribution from fluid resistive drag. In contrast, thrust was dominated by the pressure force acting on the caudal fin, as steady swimming resulted from a balance between resistive force and pressure force, with minor contributions from added-mass force and body drag forces. Therefore, added-mass force only indirectly affected the thrust generation and forward swimming speed via the caudal fin dynamics.

I. INTRODUCTION

Fish species have evolved with astonishing success in diversification and locomotion capabilities in various underwater environments [1]-[5]. Fish swimming relies primarily on undulatory motions in body and fins and has provided novel templates for underwater vehicles for higher efficiency and maneuverability than those using conventional propellers [6]-[9].

The diversification of fish species renders complex forms and functions of swimming, from which it is challenging to extract general design templates and principles for robotic emulation. Fish swimming, by its propulsion mechanism, can be categorized into two types: Body and/or Caudal Fin (BCF)

Research supported by National Science Foundation (CNS-1932130 awarded to B.C) and Army Research Office (W911NF-20-1-0226, awarded to B.C).

¹Department of Mechanical Engineering, Penn State University, University Park, PA, 16802, USA. dpl5368@psu.edu, buc10@psu.edu.

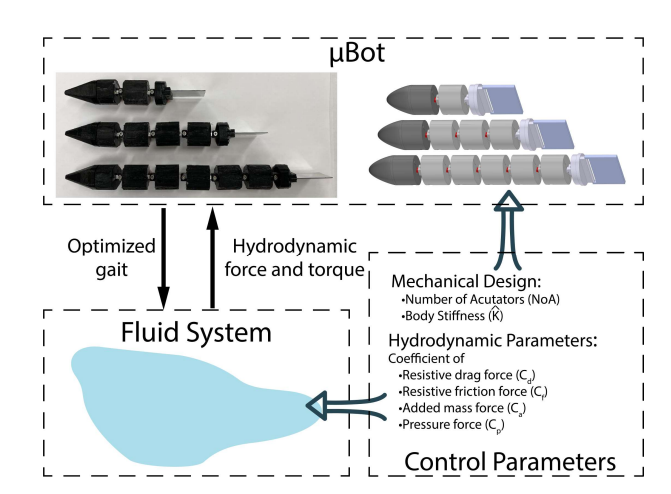


Fig. 1. Overview of this work. We explored the effect of control parameters in Number of Actuators, body stiffness, and hydrodynamic parameters (C_a , C_p , C_f , C_d).

propulsion and Median and/or Paired Fin (MPF) propulsion [10]. While BCF forms achieve higher speed and efficiency in cruising, MPF forms offer better maneuverability [11]. As 85% of fish families are estimated to use BCF propulsion [3], it is unsurprising that BCF has served as the major design template in fish-inspired robots. This template of fish swimming is primarily composed of a smooth, elongated body with caudal fin attached posteriorly, while fins along the body such as pectoral fins and dorsal fins can be considered as secondary features. Even within this parsimonious design template, there exist substantial variations such as caudal fin shape and stiffness, body slenderness, stiffness, mass distribution, and the number of actuation (or effective links). When coupled with various fluid mechanisms for hydrodynamic force generation via large possible swimming gaits, these design variations render the robot-fluid interaction problem challenging to solve or be included in the design process.

Fish or fish-inspired swimming are often studied using both experiments with biological [12], [13] or robotic fish [14], [15], or using computational simulations [16]-[18]. Experiments with robotic fish can directly reveal the swimming performance with the actual physics of robot-fluid interaction. However, these experimental setups are costly in prototyping with significant and frequent changes in mechanical design for systematic exploration in the design space. Computational Fluid Dynamic (CFD) simulation can solve Navier-Stokes equations based on known swimming kinematics and sometimes the entire fluid-structure interaction in simplified form. However, despite its high accuracy, CFD is computationally costly for systematic exploration of design space as well. Therefore, to

systematically investigate how the variations within the fishinspired design template affects the swimming gaits and performance, building an accurate and computationally efficient mathematical model for swimming is the most feasible approach.

The most widely used method for modeling fish swimming is based on the large amplitude elongated body theory (LAEBT) [19] developed by Lighthill. In the LAEBT, 3D problem is simplified as a 2D problem with potential flow, and reactive force is calculated based on the fluid in a control volume attached to the fish. Compared to the CFD solution, LAEBT predictions often have acceptable accuracy with significantly lower computational cost. In recent decades, there are also several attempts to improve the Lighthill fish swimming model and adapt it to a mobile multilink system [20].

In this work, we aimed to systematically explore the relationship among robot design properties, fluid dynamics, swimming gaits, and swimming performance in fish-inspired swimming. We first developed models and a simulation platform of a Magnetic, Modular, Undulatory Robot platform (µBot) [21], which represents a robot template for fishinspired swimming. We created a total of 36 simulation cases with distinct model parameters, namely number of actuators (NoA), body stiffness, and hydrodynamic parameters. We optimized the swimming gaits to maximize the swimming speed and analyzed the thrust generation mechanism. The rest of this paper is organized as follows. In section II, the design, mathematical modeling, simulation, and method of gait optimization of µBot are described. Section III presents the results from simulations. Discussions and future work are presented in section IV.

II. MATERIALS AND METHODS

In this section, the design, mathematical modeling, simulation setup, and method of gait optimizations of μ Bot are described. In addition, the control parameters that determine the physics of swimming are derived.

A. Robot design and actuator model

The design of μBot was described in our previous work [21], and the details relevant to modeling and simulation are provided here. The μBot is composed of a head segment, multiple body segments, a peduncle segment, and a caudal fin (Fig. 2a). A body segment has an elliptical transverse plane with a nominal depth of 13.7 mm and width of 7 mm, and a rectangular sagittal plane with nominal aspect ratio of 2 (i.e., a nominal length of 27.4 mm). The caudal fin is mounted on the peduncle segment via a torsion spring and modeled as a rigid plate with the same body depth and a thickness of 0.97mm. μBot is assumed to have a uniform density of 1.0kg/m^3 with neutral buoyancy in the simulation. Except for the last joint (peduncle-caudal fin), all other joints are actuated by a magnetic actuator with a parallel torsion spring.

Each magnetic actuator (Fig. 2b) has a coil mounted on a rotating arm (coil clamp) around a pivot joint, while the coil is placed in between two permanent magnets pointed closely to each other with identical polarity (therefore opposing each other). With voltage applied, the coil generates lateral forces,

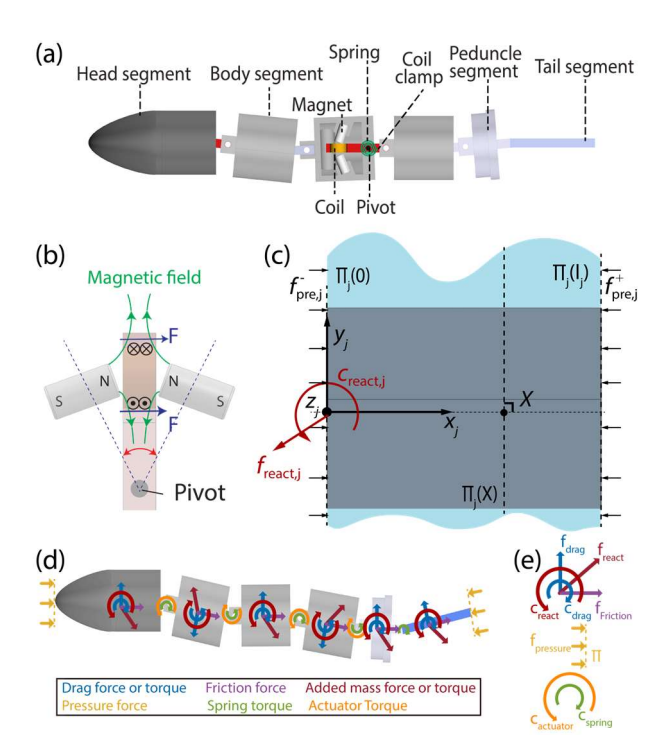


Fig. 2. Design and modeling of μ Bot. (a) Top view of μ Bot with 4 actuators. The interior actuator design of the 3^{rd} segment (actuator) is shown. (b) Details of actuator design showing the permanent magnets and coil. (c) Added-Mass Volume (AMV) and reactive forces of one segment. x and y are segmental normal and longitudinal unit vectors. (d) Scheme for the external forces and torques applied along the μ Bot (e) Examples of external forces and torques vectors with notations.

which in turn creates actuation torque via the rotating arm that rotates the subsequent segment and reversing the voltage simply reverses the torque.

To simulate torque from the actuator, a mathematical model was developed by calculating the magnetic field of the permanent magnets [23] and the coil. This model was calibrated by the torque measured experimentally at zero rotation. The model showed that both the actuator torque constant $(k_{\rm T})$ and back EMF constant $(k_{\rm EMF})$ remained nearly constant across the usable range of coil rotation. Therefore, the actuator was modeled simply as,

$$T = \frac{E - k_{\text{EMF}} \cdot \omega_{\text{joint}}}{P} \cdot k_{\text{T}}, \tag{1}$$

where T is torque generated by the actuator, E is the applied voltage, ω_{joint} is joint's angular velocity, R is the resistivity of coil, torque constant is chosen as 1.26 Nmm/A, and back EMF constant is chosen as 1.26 mV·s.

B. Modeling of hydrodynamic forces

To simulate the swimming of μ Bot, a model of hydrodynamic force was developed based on the reactive theory [19] and the resistive theory [22], following the approach used by Mathieu et al. [20] with minor revisions. Since μ Bot was neutrally buoyant, only horizontal planar motion and relevant forces and torques were considered.

We attached a mobile frame (O_j, x_j, y_j, z_j) to the segment j. The unit vector x_j is along segment longitudinal direction, y_j is along segment lateral direction, and z_j is along the

vertical direction. For any physical variable modeled as vectors, the lower index presents the body index (to which it is related). Tensor related to a body is always expressed in the mobile frame of this body.

B1. Reactive force model

Applying Lighthill's theory with potential flow assumption, we first defined a control volume attached to each segment, termed as added-mass volume (AMV). Each AMV has two boundaries Π_0 and Π_l , which are infinite planes fixed at the anterior and posterior side of each segment, respectively (Fig. 2c). The total segmental reactive force was modeled with two components: 1) added-mass force (f_{add}) due to the rate of change of fluid momentum within AMV, and 2) the pressure force $-f_{pre}^-$, f_{pre}^+ acting on the boundaries of AMV. For a given robot segment j (Fig. 2c), the total reactive wrench $F_{react,j}$, exerted by the fluid within AMV, can be written as

$$\mathbf{F}_{react,j} = \left(\mathbf{f}_{react,j}^T, \mathbf{c}_{react,j}^T\right)^T. \tag{2}$$

Here $F_{react,j}$ in R^6 is wrench and includes both force $(f_{react,j}^T)$ and torque $(c_{react,j}^T)$ components (about each joint) and is expressed in the mobile frame of j^{th} segment. Applying Newton's laws and Euler's theory to the fluids in AMV, it can be shown that,

$$f_{\text{react},j} = \frac{d}{dt} \int_0^{l_j} \mathbf{P}_j(X) dx_j + f_{pre}^- - f_{pre}^+,$$
 (3)

$$\mathbf{c}_{\text{react},j} = -\frac{d}{dt} \int_0^{l_j} \mathbf{\Sigma}_j dx_j , \qquad (4)$$

where $P_j(X)$ and $\Sigma_j(X)$ are fluid's linear momentum and angular momentum of fluid contained in slice $\Pi_j(X)$. In Lighthill's original theory, fluid outside AMV was assumed to have no velocity, so that $f_{\text{pre},j}$ can be calculated simply with the velocity of fluid within boundaries $(\Pi_j(0), \Pi_j(l_j))$ via unsteady Bernoulli's principle. However, this assumption was biased as fluid outside boundaries still has velocity, and pressure force was over-estimated. In this work, we introduced the correction coefficient C_p for pressure force. Thus, the pressure forces take the form:

$$\boldsymbol{f}_{\mathrm{pre},j} = C_p \cdot KE_j(X)x_j,\tag{5}$$

where $KE_j(X)$ denotes the kinetic energy of fluid in $\Pi_j(X)$. Evaluating (3) to (5), segmental reactive force becomes,

$$\mathbf{F}_{\text{react},j} = \begin{bmatrix} -\overline{m}_{j}l_{j}\omega_{j}v_{j} + \frac{1}{2}\overline{m}_{j}l_{j}^{2}\omega_{j}^{2} + C_{p} \cdot \frac{1}{2}\overline{m}_{j}(v_{j}^{2} - v_{j}^{2}) \\ -\overline{m}_{j}l_{j}a_{j} - \frac{1}{2}\overline{m}_{j}l_{j}^{2}\dot{\omega}_{j} \\ 0 \\ 0 \\ -\left[\frac{1}{2}\overline{m}_{j}l_{j}^{2}\left(a_{j} - \omega_{j}u_{j}\right) + \frac{1}{3}\overline{m}_{j}l_{j}^{3}\dot{\omega}_{j} + \overline{m}_{j}l_{j}u_{j}v_{j}^{2}\right] \end{bmatrix}, (6)$$

where \bar{m}_j is cross-sectional added mass, l_j is the segment length, ω_j is the angular velocity, u_j, v_j are the linear velocity of $\Pi_j(0)$ projected onto x_j, y_j , a_j is linear acceleration of $\Pi_j(0)$ projected onto y_j , and v'_j is linear velocity of boundary $\Pi_j(l_j)$ projected on y_j . According to Lighthill [24], \bar{m} is defined as

$$\overline{m}_j = C_a \cdot \frac{1}{4} \pi h_j^2 \rho_f, \tag{7}$$

where h_j is the segment depth, ρ_f is the fluid density, and C_a is the coefficient of added mass.

B2. Resistive force model

Based on Taylor's theory [22], resistive force F_{resis} takes the form of lateral drag force and longitudinal friction force,

$$F_{\text{resis},j} = -\frac{1}{2}\rho_{f} \begin{bmatrix} C_{f} \cdot P_{j} \cdot l_{j} \cdot |u_{j}| u_{j} \\ C_{d}h_{j} \int_{0}^{l_{j}} |v_{x,j}| v_{x,j} dx_{j} \\ 0 \\ 0 \\ 0 \\ C_{d}h_{j} \int_{0}^{l} |v_{x,j}| v_{x,j} \cdot x dx_{j} \end{bmatrix},$$
(8)

where P_j is segment perimeter, C_f , C_d are friction and drag coefficients that are Reynolds-number dependent, u_j is segment's longitudinal velocity and $v_{x,j}$ is the lateral velocity of the slice of fluid at longitudinal coordinate x.

C. Dimensionless parameters (control parameters) of swimming and robot-fluid interaction

Fish swimming involves complex interactions between the fish's body and the surrounding fluids, posing an inherent fluid-structure interaction (FSI) problem. Here, we derive several dimensionless parameters that effectively "control" the nature of this interaction in addition to the gait parameters (which are optimized). Dimensionless variables (unit \hat{x} , time \hat{t} , longitudinal velocity \hat{u} , lateral velocity \hat{v} , angular velocity $\hat{\omega}$, and angular acceleration $\hat{\beta}$) were defined as,

$$\hat{x}_j = \frac{x}{l_i}, \quad \hat{t} = ft, \quad \hat{u} = \frac{u}{U}, \quad \hat{v} = \frac{v}{f\bar{A}}, \quad \hat{\omega} = \frac{\omega}{f}, \quad \hat{\beta} = \frac{\dot{\omega}}{f^2}, \quad (9)$$

where f, U, \bar{A} denote the undulatory frequency, the average cruising speed and segment's average lateral displacement, and all three parameters are updated during the optimization. The dimensionless model of hydrodynamic force is,

$$\begin{bmatrix} \frac{f_{\text{react}}}{\frac{\pi}{4}\rho_{f}l^{2}h^{2}f^{2}} \\ \frac{c_{\text{react}}}{\frac{\pi}{4}\rho_{f}l^{3}h^{2}f^{2}} \end{bmatrix} = C_{a} \cdot \begin{bmatrix} \frac{\bar{A}}{l}\widehat{\omega}\hat{v} + \frac{1}{2}\widehat{\omega}^{2} + C_{p}\left(\frac{\bar{A}}{l}\widehat{v}\widehat{\omega} - \frac{1}{2}\widehat{\omega}^{2}\right) \\ -\frac{\bar{A}}{l}\widehat{\alpha} - \frac{1}{2}\hat{\beta} \\ 0 \\ 0 \\ 0 \\ \frac{1}{2}\frac{\bar{A}}{l}\widehat{\alpha} - \frac{1}{2}\frac{U}{lf}\widehat{u}\widehat{\omega} + \frac{1}{3}\hat{\beta} + \frac{U}{lf}\frac{\bar{A}}{l}\widehat{u}\widehat{v} \end{bmatrix}, (10)$$

$$\begin{bmatrix} \frac{f_{\text{resis}}}{\frac{\pi}{4}\rho_{f}l^{2}h^{2}f^{2}} \\ \frac{c_{\text{resis}}}{\frac{\pi}{4}\rho_{f}l^{3}h^{2}f^{2}} \end{bmatrix} = -\frac{2}{\pi} \cdot \begin{bmatrix} C_{f} \cdot AR \cdot \left(\frac{u}{lf}\right)^{2} |\hat{u}|\hat{u} \\ C_{d} \cdot AR \cdot \left(\frac{\bar{A}}{l}\right)^{2} \int_{0}^{1} |\hat{V}| \hat{V} d\hat{x} \\ 0 \\ 0 \\ 0 \\ C_{d} \cdot AR \cdot \left(\frac{\bar{A}}{l}\right)^{2} \int_{0}^{1} |\hat{V}| \hat{V} \hat{x} d\hat{x} \end{bmatrix}, \quad (11)$$

where $\hat{V} = \hat{v} + \frac{l}{\bar{A}}\hat{x}\hat{\omega}$ and $AR = \frac{l}{h}$ is body segmental aspect ratio.

TABLE I. SETTING OF CONTROL PARAMETERS

Control Parameters	Values of Control Parameters					
Number of actuators NoA	2		4		6	
Normalized Stiffness \hat{K} , (Nmm/rad)	High 1.00 16		$\frac{\text{Medium}}{0.75}$ $\frac{16}{}$		Low 0.50 16	
Hydrodynamic Model	$HM-1$ $C_a = 0$ $C_p = 0$		M-2 = 1 = 0	$ \begin{array}{c} \text{HM-}:\\ C_a = \\ C_p = 0 \end{array} $	1	$HM-4$ $C_a = 1$ $C_p = 1$

From the dimensionless model, we identified two types of dimensionless parameters: 1) those that need to be defined *a priori* before starting simulation and optimization, such as AR, C_a , C_p , C_f , C_d , which are the 'control parameters' of the swimming physics, and 2) those that will be obtained after gait optimization, such as $\frac{A}{l}$, $\frac{U}{lf}$.

To investigate the effects of hydrodynamic parameters, which change with the Reynolds number, we created four hydrodynamic models (Hydro Model or HM) with different combinations of C_p and C_a (Table 1). Hydro Model-1 represents a model in which µBot only experiences resistive force from fluid due to boundary layer effects (or circulatorybased frictional and drag forces). Hydro Model-2 represents a model containing resistive force and part of the reactive force with $C_p = 0$. In this model, we assume there is no difference in fluid velocity between both sides of boundaries of AMV. Therefore, pressure force f_{pre}^- and f_{pre}^+ are zero. Hydro Model-3 denotes a model containing all resistive force and reactive force components with $C_p = 0.5$. Hydro Model-4 denotes a classical hydro-dynamic model containing all resistive force and reactive force components with $C_p = 1$. From Hydro Model-2 to Hydro Model-4, we gradually increase the coefficient of pressure force to explore how it affects robot swimming.

The effects of two body design parameters were investigated: 1) the number of actuators (NoA) or the number of body segments, as the μ Bot is a multilink robot, and 2) torsion spring stiffness (K_i). For an N-segment μ Bot model, K_i can be written as,

$$K_{j} = \begin{cases} AR^{4} \cdot \hat{K} & i = 1, 2, ..., N - 2 \\ AR^{4} \cdot 5\hat{K} & i = N - 1 \end{cases}$$
 (12)

where K_i is the stiffness for torsional spring in i^{th} joint and \widehat{K} is the normalized spring stiffness. With a normalized spring stiffness \widehat{K} , the effects of spring and AR can be isolated. The caudal fin joint stiffness is 5 times of the rest joint stiffness to match the actual robot design.

In total, AR, (C_f, C_d) , HM, \widehat{K} and NoA are five key dimensionless parameters, or Control Parameters (CPs). In this study, we investigated the effects these CPs (except the \widehat{K}) by creating a total of 36 simulations cases according to Table 1.

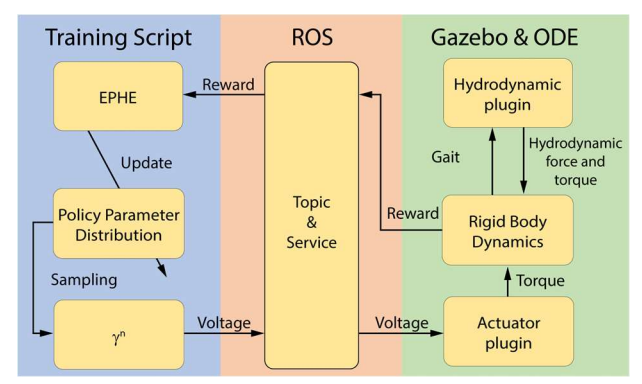


Fig. 3. Schematics of the simulation platform.

D. Gait Optimization

With the determined set of CPs, we optimized the μ Bot's actuator voltage signals to identify the swimming gaits that maximize the forward swimming speed for each simulation case. In this work, we generated the voltage signal $E_j(t)$ sent to j^{th} actuator according to,

$$E_{j}(t) = \begin{cases} e_{j} \sin(2\pi f_{in}t), & j = 1\\ e_{j} \sin(2\pi (f_{in}t + \Psi_{j})), & j = 2 \dots NoA \end{cases}$$
(13)

where e_j is voltage amplitude, Ψ_j is the initial phase of voltage, and f_{in} is the frequency of input signal. Given this definition, the optimization parameter vector γ , which governs voltage signal, can be constructed as,

$$\gamma = [e_1, \Psi_2, e_2 \dots \Psi_{NOA}, e_{NOA}, f_{in}].$$
 (14)

In this work, a policy gradient-based reinforcement learning (RL) method, i.e., EM-based Policy Hyper Parameter Exploration (EPHE) [25], was used to optimize the swimming gaits of swimming. In EPHE, policy parameters γ is sampled from probability distribution $p(\gamma|\eta,\sigma^2)$, where η,σ are the hyperparameter vectors composed of mean value and standard deviation of the probability distribution. To obtain a good sampling performance, only the policy parameters from the best N rollouts (trajectories with highest N rewards) in total M rollouts are taken for updates. Hyperparameters are updated

$$\eta = \frac{\sum_{i=1}^{N} [R(\gamma^i) \gamma^i]}{\sum_{i=1}^{N} R(\gamma^i)},$$
(15)

$$\sigma = \sqrt{\frac{\sum_{i=1}^{N} [R(\gamma^{i}) (\gamma^{i} - \eta)^{2}]}{\sum_{i=1}^{N} R(\gamma^{i})}},$$
 (16)

where $R(\gamma^i)$ is the reward of the i^{th} rollout.

Empirically, μ Bot took less than 2 seconds for acceleration and got into a steady swimming phase. Therefore, we set μ Bot to swimming for 6 seconds and used the average speed within the last 2 seconds as the reward of learning.

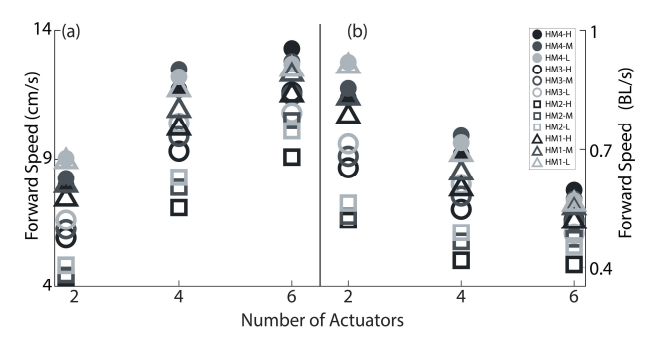


Fig. 4. Optimized forward speed of all 36 cases. 'H', 'M' and 'L' denote high stiffness, medium stiffness, and low stiffness. (a) shows the absolute optimized forward speed for all 36 cases. (b) shows the optimized forward speed in body-length per second (BL/s).

E. Robot Simulation Setup

Next, the above hydrodynamic models and EPHE algorithm were used to create a simulation platform, which was composed of three parts: Gazebo and Open Dynamic Engine (ODE), training script, and Robot Operating System (ROS).

In this paper, the combination of Gazebo and ODE was used as a robot simulator while a hydrodynamic plugin and an actuator plugin were implemented in it. At a given timestep t_k , ODE calculated hydrodynamic force (F_{react} , F_{resis}) based on kinematic variables from t_{k-1} , generated excitation torque based on $E_i(t_k)$, and handled motion of equation for µBot by simulating rigid body dynamics. The training script contained learning algorithm and generated voltage signals for actuators. To integrate the training script into the Gazebo and ODE simulator, we used ROS for action controlling and data passing. During the simulation, training script used EPHE to sample policy parameters, generated voltage signals, and sent signals to Gazebo via ROS nodes and services. Then, Gazebo calculated robot dynamics and recorded robot gait information. Once one simulation rollout was done, Gazebo sent the reward to training scrip via ROS nodes and services (Fig. 3).

III. RESULTS

In the current work, we investigated the effects of NoA, hydrodynamic coefficients of reactive force (four combinations of C_a and C_p), and stiffness \widehat{K} . The remaining

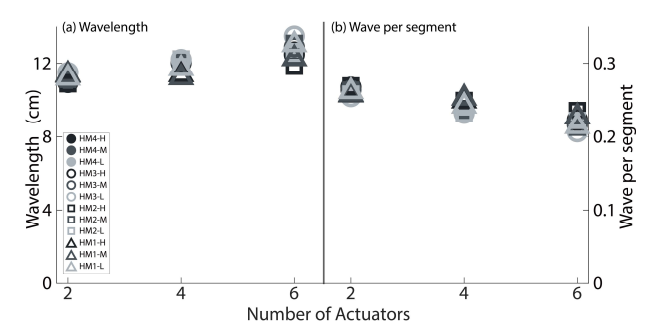


Fig. 5. Wavelength of optimized gaits remained approximately constant in 36 cases. (a) shows the wavelengths of optimized gait for all 36 cases with scales on the left. (b) shows the wave per segment of optimized gait for all 36 cases with scales on the right.

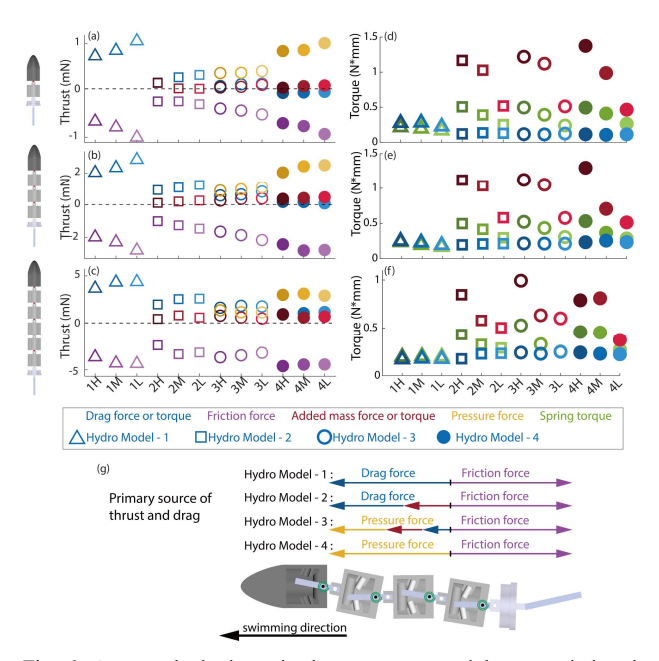


Fig. 6. Average hydrodynamic thrust over an undulatory period and torques applied at tail in all cases. On x axis, '1', '2', '3', '4' denote Hydro Model-1, Hydro Model-2, Hydro Model-3, Hydro Model-4 and 'H', 'M', 'L' denotes high stiffness, medium stiffness, and low stiffness. (a)(b)(c) shows total thrust generated from different type of force with 2 actuators, 4 actuators and 6 actuators. (d)(e)(f) shows torque applied tail with 2 actuators, 4 actuators and 6 actuators. (g) scheme of primary source of thrust and friction during steady state swimming.

control parameters were fixed as AR=2, $C_f=0.06$, and $C_d=2.25$. To optimize the forward swimming, we performed 50 rollouts in each episode and picked the 25 best performing rollouts to update the actuation policy. In each training session, we have updated the policy 40 times. For each simulation case, we repeated the training sessions 3 times with random initial conditions. The repeated training sessions gave similar final reward values (forward speeds) with negligible differences. In each simulation case, with the optimized voltage signal, an undulatory gait in the form of a backward traveling wave emerges from the fluid-structure interaction.

A. Effects of number of actuators (NoA)

With a higher NoA, the optimized forward speed increases with NoA (Fig. 4a), however, the forward speed per body-length decreases, suggesting the gain of forward speed from adding more actuators or body segments diminishes. This trend is independent of the hydrodynamic models (with different combinations (C_a, C_p)) or spring stiffness of \widehat{K} .

Fig. 5 shows the dependence of optimized gait wavelength on NoA. The wavelengths remain approximately constant at 12 cm regardless of the robot length and the averages of wave per body segment remain approximately 0.25, i.e., a full wave spans 4 body segments. Unlike observations in biological fish, which show a positive correlation between wavelength and body length [26], our results indicate that the wavelength of optimized swimming in μ Bots is only weakly correlated to the selected control parameters, NoA, hydrodynamic parameters, and body stiffness.

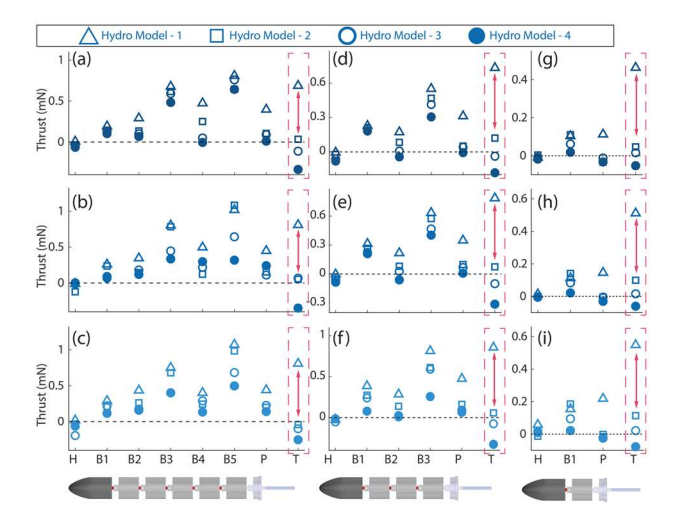


Fig. 7. Distribution of thrust from resistive drag force along $\mu Bots$ for all 36 cases and red boxes and arrows shows big difference at tail among different Hydro Models. Four different hydrodynamic models are distinguished by shapes: triangles for Hydro Model-1 cases, squares for Hydro Model-2 cases, hollow circles for Hydro Model-3 cases and filled circles for Hydro Model-4 cases. Columns from left to right denote thrust distribution with 6 actuators, 4 actuators, and 2 actuators. Rows from top to bottom show thrust distribution with high stiffness, medium stiffness and low stiffness. In each plot, x axis denotes different segments, while 'H', 'B', 'P' and 'T' denote head segment, body segment, peduncle segment and tail segment, respectively.

B. Effects of hydrodynamic parameters

Fig. 6 shows the average hydrodynamic thrusts over an undulatory period (summing across all segments) and torques applied on the caudal fin in all cases. From Fig. 6a to Fig. 6c, resistive friction force is the dominant force resisting the motion along the swimming direction. In steady state swimming, the resistive friction force is balanced by resistive drag force in HM-1, by resistive drag force (primary) and added-mass force (secondary) in HM-2, and by caudal-fin pressure forces (primary), resistive drag and added-mass forces (both secondary) in HM-3 and HM-4. Note that the pressure force, being the dominant mechanism for thrust generation, is mainly from the caudal fin, indicating the importance of caudal-fin design and dynamics in thrust generation and swimming speed [27].

Fig.7a to Fig.7i further shows the distribution of thrust from resistive drag force along the body segments of μ Bots. Unlike the pressure force, the drag force from body segments contribute to the thrust generation and has a minor difference under different Hydro Model, while the caudal-fin drag force has dramatically difference under different Hydro Model and has negligible contribution to thrust in all cases except for the case with HM-1 (shown in Fig 7 with red boxes and arrows).

While added-mass forces do not contribute significantly to thrust generation, the added-mass torque, on the other hand, dominates the caudal fin dynamics (Fig. 6d to Fig. 6f). It can be seen that added-mass torque has a similar magnitude to spring torque, indicating a balance in a near resonant state (except the low spring stiffness cases). Results show that µBot, under hydrodynamic model with added-mass forces (HM-2, HM-3, HM-4) and without added-mass forces (HM-1), has categorically different caudal-fin kinematics, which lead to different thrust generation mechanisms. Therefore,

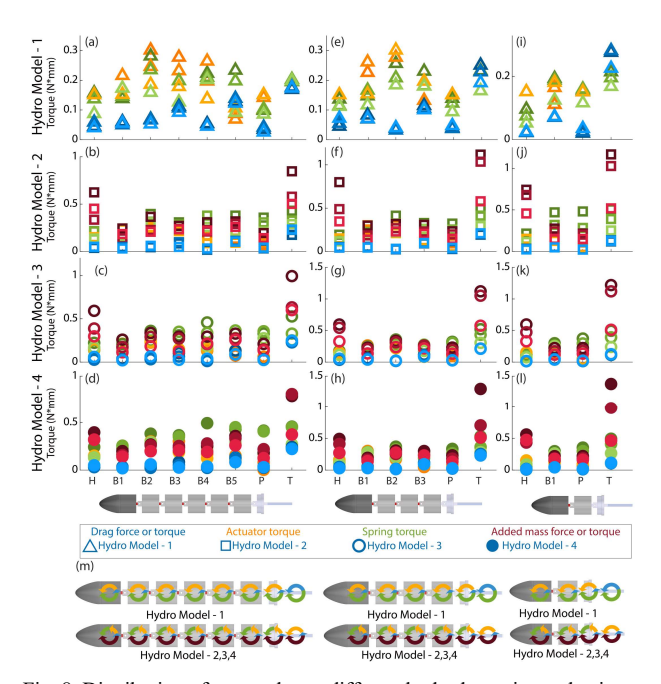


Fig. 8. Distribution of torque due to different hydrodynamic mechanisms along body. From (a) to (l), columns from left to right denotes torque distribution with 6 actuators, 4 actuators, and 2 actuators. Rows from top to bottom shows torque distribution under different hydrodynamic models. (m) Schemes that shows torques applied at each segment.

added-mass force indirectly affects the thrust generation and swimming speed via the caudal fin dynamics.

In addition, Fig. 8a to Fig.8l show that the actuation torque, fluid added-mass torque, and spring torque have comparable magnitudes at the robot body. In contrast, the contributions from the resistive drag force are again negligible. The results indicate that the robot gait, including both body and caudal-fin gaits, are dominated by the interaction between the robot dynamics and the reactive hydrodynamic forces.

IV. DISCUSSIONS AND FUTURE WORK

In summary, our results show that increasing NoA (i.e., increasing robot length and the number of actuators) increases the optimized forward swimming speed, however, with a diminishing gain, as the forward speed per body length decreases. Note that among all the 36 cases, the μ Bot with NoA = 6, Hydro Model-4 model, and highest stiffness has the fastest forward speed of 13.3cm/s or 0.60BL/s, and the μ Bot with NoA = 2, Hydro Model-2 model, and high stiffness has the lowest forward speed of 4.32cm/s or 0.37BL/s.

Interestingly, via examining the contributions of different hydrodynamic mechanisms, we found fundamentally different roles of fluid added-mass towards thrust generation and gait generation: the added-mass *force* had a negligible contribution to the thrust generation, while added-mass *torque* dominates the gait generation in both caudal-fin and body segments, together with spring torque and actuator torque. The resistive drag force, on the other hand, has negligible contribution towards the gait generation, however, it contributes to the thrust mainly from the body segments. These understandings will be crucial for understanding the experimental data of µBot, including performing [21] robot

system identification and possible model-based reinforcement learning in the future.

Finally, note that the current analysis does not fully explore the specific effects of body and caudal fin stiffness \widehat{K} , because only three sample values were used. Although the optimized swimming speed seems to only depend weakly on the stiffness, the swimming gait and efficiency could have greater dependence. In future work, we plan to perform a more comprehensive study on the effects of body and caudal-fin spring stiffness. Furthermore, in this work, we only examined the effects of three control parameters out of the five derived (see in II.C). In future work, we will continue to explore the effects of these control parameters and investigate the relationship among body morphologies, dynamics, swimming gaits, and swimming performance in fish-inspired swimming. In addition, we also plan to perform system identifications (e.g., identifying the hydrodynamic parameters) using experimental data of µBots.

REFERENCES

- [1] R. Bainbridge, "The speed of swimming of fish as related to size and to the frequency and amplitude of the tail beat," *J. Exp. Biol.*, vol. 35, no. 1, pp. 109–133, 1958.
- [2] J. J. Videler, and C. S. Wardle, "Fish swimming stride by stride: speed limits and endurance," *Rev. Fish Biol. Fish.*, vol. 1, no. 1, pp. 23–40, 1991
- [3] J. J. Videler, Fish Swimming. London, U.K: Chapman and Hall, 1993.
- [4] L. Fuiman, and R. Batty, "What a drag it is getting cold: partitioning the physical and physiological effects of temperature on fish swimming," *J Exp Biol.*, vol. 200, no.12, pp. 1745-1755, 1997.
- [5] M. Gazzola, M. Argentina, and L. Mahadevan, "Scaling macroscopic aquatic locomotion," *Nat. Phys.*, vol. 10, no. 10, pp. 758–761, 2014.
- [6] M. S. Triantafyllou, and G. S. Triantafyllou, "An efficient swimming machine," Sci. Am., vol. 272, no. 3, pp. 64–70, 1995.
- [7] R. K. Katzschmann, J. DelPreto, R. MacCurdy, and D. Rus, "Exploration of underwater life with an acoustically controlled soft robotic fish," *Sci. Robot.*, vol. 3, no. 16, 2018.
- [8] K. H. Low, "Current and future trends of biologically inspired underwater vehicles," 2011 Defense Science Research Conference and Expo (DSR), 2011, pp. 1-8.
- [9] S.-J. Park et al., "Phototactic guidance of a tissue-engineered soft robotic ray," *Science*, vol. 353, no. 6295, pp. 158–162, 2016.
- [10] M. Sfakiotakis, D. M. Lane, and J. B. C. Davies, "Review of fish swimming modes for aquatic locomotion," *IEEE J. Ocean. Eng.*, vol. 24, no. 2, pp. 237–252, 1999.
- [11] W. Webb, "Form and Function in Fish Swimming," Sci. Am., vol. 251, no. 1, pp. 72-83, 1984.
- [12] K. D'Août and P. Aerts, "A kinematic comparison of forward and backward swimming in the eel Anguilla anguilla," *J. Exp. Biol.*, vol. 202, no. 11, pp. 1511–1521, 1999.
- [13] E.G. Drucker, and G.V. Lauder, "A hydrodynamic analysis of fish swimming speed: wake structure and locomotor force in slow and fast labriform swimmers," *J Exp Biol.*, vol. 203, no. 16, pp. 2379-2393, 2000.
- [14] R.K. Katzschmann, A.D. Marchese, and D. Rus, "Hydraulic autonomous soft robotic fish for 3d swimming," *Experimental Robotics*, pp. 405-420.
- [15] J. Yu, M. Tan, S. Wang, and E. Chen, "Development of a biomimetic robotic fish and its control algorithm," in *IEEE Trans. Syst. Man Cybern. Cybern.*, vol. 34, no. 4, pp. 1798-1810, Aug. 2004.
- [16] J. Chen, W.O. Friesen, and T. Iwasaki, "Mechanisms underlying rhythmic locomotion: body–fluid interaction in undulatory swimming," *J Exp Biol.*, vol. 214, no. 4, pp. 561-574, 2011.

- [17] M. Gazzola, M. Argentina, and L. Mahadeva, "Gait and speed selection in slender inertial swimmers," *Proc. Natl. Acad. Sci. U. S. A.*, vol. 112, no. 13, pp. 3874–3879, 2015.
- [18] K.L. Feilich, and G.V. Lauder, "Passive mechanical models of fish caudal fins: effects of shape and stiffness on self-propulsion," *Bioinspir. Biomim.*, vol. 10, No. 3.
- [19] M.J. Lighthill, "Large-amplitude elongated-body theory of fish locomotion," *The Royal Society*, vol. 179, no. 1055, pp. 125-138, 1971
- [20] M. Porez, F. Boyer, and A.J. Ijspeert, "Improved Lighthill Fish Swimming Model for Bio-Inspired Robots: Modeling, Computational Aspects and Experimental Comparisons," *The International Journal of Robotics Research*, vol 33, no. 10, 2014, pp. 1322-1341.
- [21] H. Deng, P. Burke, D. Li, and B. Cheng, "Design and experimental learning of swimming gaits for a magnetic, modular, undulatory robot," *IEEE/RSJ Int. Conf. Intell. Robot. Syst.*, 2021, pp. 9562–956.
- [22] G. Taylor, "Analysis of the swimming of long and narrow animals". Proceedings of the Royal Society of London. Series A, Mathematical and Physical Sciences, vol 214, no. 1117, 1952, pp. 158-183.
- [23] A. Caciagli, R. J. Baars, A.P. Philipse and B. W.M. Kuipers. "Exact expression for the magnetic field of a finite cylinder with arbitrary uniform magnetization." *Journal of Magnetism and Magnetic Materials*, vol. 456, 2018, pp. 423–432.
- [24] M.J. Lighthill, "Aquatic animal propulsion of high hydromechanical efficiency". *Journal of Fluid Mechanics*, Vol 44, part 2, 1970, pp. 265-301.
- [25] J. Wang, E. Uchibe and K. Doya. "EM-based policy hyper parameter exploration: application to standing and balancing of a two-wheeled smartphone robot," *Artificial Life and Robotics*, vol 21, no. 1, 2016, pp. 125-131.
- [26] P.W. Webb, P.T. Kostecki, "The effect of size and swimming speed on locomotor kinematics of rainbow trout," *J Exp Biol.*, vol. 109, pp. 77-95, 1984.
- [27] E.D. Tytell and G.V. Lauder, "The hydrodynamic of eel swimming", J. Exp. Biol., vol. 207, pp. 1825-1841, 2004.